Mid-infrared laser-induced thermal grating spectroscopy of hot water lines for flame thermometry

Hot, Dina; Sahlberg, Anna Lena; Aldén, Marcus; Li, Zhongshan

Published in:
Proceedings of the Combustion Institute

DOI:
10.1016/j.proci.2020.06.289

2021

Available online at www.sciencedirect.com

ScienceDirect

Proceedings of the Combustion Institute 38 (2021) 1885–1893

Proceedings of the Combustion Institute

www.elsevier.com/locate/proci

Mid-infrared laser-induced thermal grating spectroscopy of hot water lines for flame thermometry

Dina Hot, Anna-Lena Sahlberg*, Marcus Aldén, Zhongshan Li

Division of Combustion Physics, Lund University, P.O. Box 118, S-221 00 Lund, Sweden

Received 7 November 2019; accepted 20 June 2020
Available online 4 September 2020

Abstract

In this work we report the impact of using mid-infrared laser-induced thermal grating spectroscopy (IR-LITGS) for temperature measurements in flames by probing hot water lines. The measurements have been performed in the product zone of laminar atmospheric CH_4/H_2/air flat flames with equivalence ratio ranging between 0.6 and 1.05. LITGS is a technique based on thermalization through collisions of the excited molecules for generation of a laser-induced grating, which then decays through thermal diffusion. As such, it tends to have limited application in atmospheric flames compared to flame measurements at elevated pressures due to the faster decay at low gas densities. However, by using mid-IR pump laser beams, it enables the generation of laser-induced gratings with large grating spacing, resulting in strong signal intensities and long signal durations. Single-shot IR-LITGS signals were recorded in the different CH_4/H_2/air flames that covered a temperature range between 1500 and 1800 K. To test the accuracy, the IR-LITGS flame temperature measurements were compared with laser Rayleigh scattering measurements and the result were in good agreement with each other. The IR-LITGS flame temperature measurements show a repetitive single-shot temperature precision better than 1% and an accuracy of 2.5% of the flame temperature. An IR-LITGS excitation scan of water in the flame shows that some ro-vibrational transitions exhibit no IR-LITGS signal, probably due to less efficient collisional energy transfer mechanism. This is important when deciding the wavelength to use for IR-LITGS flame temperature measurements using water absorption.

Keywords: Laser-induced thermal grating spectroscopy; Mid-infrared; Atmospheric flame; Temperature; Water

1. Introduction

Temperature is one of the most important parameters in understanding combustion phenomena. Many laser techniques have been developed for non-intrusive flame temperature measurements in combustion environments, such as laser-induced fluorescence [1], two-line atomic fluorescence [2] and degenerate four-wave mixing (DFWM) [3]. Coherent anti-Stokes Raman scattering (CARS) has been widely employed for temperature measurements in combustion environments with high precision and accuracy [4]. Laser

* Corresponding author.
E-mail address: anna-lena.sahlberg@forbrf.lth.se (A.-L. Sahlberg).

https://doi.org/10.1016/j.proci.2020.06.289

Rayleigh scattering (LRS) measures the elastic scattering from molecules, which can be converted to temperature with the pre-knowledge of the major species concentration and the Rayleigh cross sections [5,6].

Laser-induced thermal grating spectroscopy (LITGS) is a promising laser technique for flame thermometry. In a typical LITGS experiment, two coherent pump beams from a pulsed laser are crossed in the measurement point, creating an interference pattern. Absorption of the pump beams and subsequent collisional quenching of the excited molecules leads to temperature/density variations. Thus, a periodic modulation of the refractive index in the medium, and a laser-induced grating (LIG), is formed [7]. In addition, the rapid density changes in the medium generates a standing acoustic wave. A non-resonant LIG can also be formed by electrostriction, but this effect is often negligible for cases of strong absorption. The formation and time-evolution of the LIG can be monitored by aligning a probe laser beam (usually a continuous-wave laser) across the LIG at the Bragg angle. The partial diffraction of the probe beam off the LIG forms the LITGS signal [7].

The LITGS signal oscillates at the frequency $f_{osc}=c_s/\Lambda$, where c_s is the speed of sound in the gas and Λ is the grating spacing. Therefore, the transient LITGS signal can be used for measurements of the sound speed in a gas [8] and the gas temperature can be derived if the gas composition in the measurement volume is known. Both electrostrictive and thermal LIGs has been applied to temperature measurements in e.g. flames [9–11], engines [12,13] and shock-tubes [14].

The precision of LITGS temperature measurements relies on accurate determination of the oscillation frequency. The time decay of the LITGS signal is given by $\tau_{th} =(\Lambda/2\pi)^2/\chi$ [15], where χ is the thermal diffusivity, which is strongly dependent on the gas density. LITGS temperature measurements in atmospheric pressure flames are often limited by the fast signal decay in high temperature environments, which in turn affects the precise determination of the LITGS oscillation frequency. Therefore, the main application of LITGS for temperature measurements in combustion environments has been performed at high pressures; where many other laser techniques suffer from the increased collisional quenching, the LITGS signal intensity and precision increases at elevated pressures. Hayakawa et al. [16] measured the flame temperature in laminar $CH_4/O_2/N_2$ flames at pressures up to 1 MPa using OH absorption lines for LITGS generation. De Domenico et al. [17] demonstrated LITGS measurements using weak water absorption lines at 1064 nm for flame temperature measurements at 1–6 bar, showing how the signal intensity and the quality of the temperature measurement improved drastically with increasing pressure. However, the quality of the LITGS signals recorded at atmospheric pressure flames was low.

Another way to increase the time duration of the LITGS signals is to increase the grating spacing, since the time decay $\tau_{th}\propto\Lambda^2$. The grating spacing is determined by $\Lambda= \lambda_{pump}/2\sin(\theta/2)$, where λ_{pump} is the pump laser wavelength and θ is the crossing angle between the pump beams. For practical alignment purposes, there is a limit to how small the crossing angle can be. The other way to increase the grating spacing is to use a longer wavelength pump laser. Mid-infrared LITGS (IR-LITGS) using molecular ro-vibrational transitions around 3 μm has been demonstrated for detection of C_2H_2 in gas flows [18]. Water is an attractive target for mid-infrared absorption since it is a main combustion product commonly present in large concentrations. The first flame temperature measurements using water-line IR-LITGS was performed by Sahlberg et al. [19], showing the potential of the technique for rich atmospheric pressure flames. However, this experiment still showed fairly rapid signal duration, which limited the precision of the temperature measurement. In this paper, we demonstrate an improved water-line IR-LITGS experiment for flame thermometry in atmospheric pressure lean CH_4/H_2/air flames. The large grating spacing in this setup contributed to a strongly improved signal-to-noise ratio and a much higher precision in the temperature measurement, for both single-shot and time-averaged signals. To investigate the accuracy, the IR-LITGS flame temperature measurements are compared with LRS temperature measurements. These results show that IR-LITGS can be applied for accurate, precise single-shot flame temperature measurements at atmospheric pressure.

2. Experimental arrangement

2.1. IR-LITGS measurements

A schematic of the IR-LITGS setup is shown in Fig. 1. The laser system has been described elsewhere [20] and only a brief description is given here. The 2nd harmonic of an injection-seeded Nd:YAG laser (Spectra Physics, PRO 290-10) at 532 nm is used to pump a dye laser (Sirah, PRSC-D-18, with dye LDS 798). The mid-IR laser radiation around 3.1 μm was produced by difference frequency mixing the Nd:YAG output at 1064 nm with the dye laser output at ~792 nm in a $LiNbO_3$ crystal. The generated mid-IR laser light was amplified in a $LiNbO_3$ crystal pumped with another part of the residual 1064 nm beam, producing tunable mid-IR radiation with pulse energies around 6 mJ and pulse duration of 3–4 ns. The linewidth of the mid-IR laser is 0.025 cm^{-1} [21]. The mid-IR laser beam was spatially overlapped with a HeNe beam to facilitate alignment. A 50/50 CaF_2 beam splitter split the

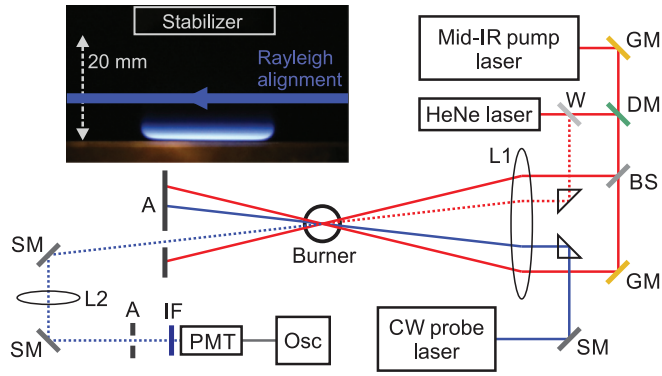

Fig. 1. Schematic view of the IR-LITGS setup. GM: gold mirror, SM: silver mirror, DM: dichroic mirror, W: CaF_2 window, BS: CaF_2 beam splitter (50/50), CaF_2 lenses L1: $f = 500$ mm, L2: $f = 750$ mm, A: aperture, IF: interference filter 457.9 ± 10 nm, PMT: photomultiplier tube, OSC: oscilloscope. The photograph shows the CH_4/air flame at Φ=1 (Flame 2). The LRS alignment is illustrated in the flame image.

mid-IR laser beam into two pump beams, which were crossed and focused at ~2.8° crossing angle by a 2″ $f = 500$ mm CaF_2 lens, resulting in a grating spacing of 63.5 μm and a measurement volume of $16 \times 0.5 \times 0.5$ mm^3. A CW solid state laser (Laserglow Tech., LRS-0457) with a wavelength of 457 nm and output power of ~170 mW was used as the probe laser. The probe laser beam was aligned to cross the LIG at the Bragg angle 0.2°. A fraction of the HeNe beam reflected from a CaF_2 window was aligned to cross the LIG at the opposite Bragg angle from the probe laser, thus tracing the signal beam path. The signal beam was collimated by a $f = 750$ mm CaF_2 lens and directed towards a photomultiplier tube (PMT, Hamamatsu H6780-04) connected to an oscilloscope (LeCroy WaveRunner 6100, 1 GHz). An interference filter ($457.9 \text{ nm} \pm 10$ nm) was placed in front of the PMT to suppress stray light.

2.2. Flames

The IR-LITGS measurements were performed in laminar, flat CH_4/H_2/air flames stabilized on a modified Perkin-Elmer burner with an inner porous plug diameter of 25 mm surrounded by a N_2 co-flow, resulting in a total diameter of 45 mm. The addition of hydrogen increased the flammability and made it possible to produce stable lean flames with low flame temperatures, thus allowing measurements in a wider temperature range. Table 1 shows the flame composition and equivalence ratio (Φ) of the 8 different flames studied here. The measurements were performed in the product zone at 8 mm height above the burner (HAB). A bluff-body stabilizer was placed 20 mm above the burner surface. The fuel and air flows were controlled by Bronkhorst mass flow controllers. A 5 l/min nitrogen co-flow was used to shield the flames.

A program called CEA (Chemical Equilibrium with Applications [22]) was used to simulate the flame composition. Table 2 shows the simulated major species concentrations in the product zone of flames 1–8. Since the exact flame composition depends on the flame temperature, an iterative process was used together with the LRS flame temperature measurement in order to simulate the gas composition at the correct temperatures.

Table 1
Fuel/air flows in flames 1–8. The total flow rate for all flames was 5 l/min.

Flame	CH_4 flow [l/min]	H_2 flow [l/min]	Air flow [l/min]	Φ
1	0.497	0	4.500	1.05
2	0.475	0	4.530	1
3	0.432	0	4.575	0.9
4	0.381	0.164	4.455	0.9
5	0.342	0.146	4.515	0.8
6	0.264	0.264	4.470	0.7
7	0.176	0.410	4.410	0.6
8	0.136	0.544	4.320	0.6

Table 2
Simulated major species mole fractions (x_i) for flames 1–8 [22].

Flame	x_{N2}	x_{H2O}	x_{CO2}	x_{O2}
1	0.7198	0.1941	0.0847	0.0014
2	0.7197	0.1878	0.0878	0.0047
3	0.7233	0.1725	0.0855	0.0187
4	0.7203	0.1804	0.0807	0.0186
5	0.7260	0.1628	0.0739	0.0373
6	0.7296	0.1519	0.0612	0.0573
7	0.7320	0.1443	0.0460	0.0777
8	0.7275	0.1559	0.0394	0.0771

2.3. LRS measurements

The flame temperature was measured using an LRS setup. The 457 nm CW laser of ~170 mW, with a diameter of 2 mm, was sent through the

Table 3
Refractive index (n) and Rayleigh cross section (σ_R) at 457 nm for different gases.

Species	$(n\text{-}1) \times 10^{-3}$	σ_R
($\times 10^{-27}$ cm^{-2})		
N_2	0.301[a]	1.1367
O_2	0.256[b]	0.8192
H_2O	0.278[c]	0.9655
CO_2	0.453[d]	2.5769

[a] From [25].
[b] From [27].
[c] Estimated from [6,26].
[d] From [28].

flame at 8 mm HAB, as illustrated in Fig. 1. The Rayleigh scattering from the laser beam was collected by an EMCCD camera (Andor Luca^{EM} R DL-604M-OEM) equipped with a Nikon (50 mm, f/2.8) camera lens. During the measurements, the exposure time of the camera was set to 0.1 s, and the EM gain to 10. Each signal was recorded as the average of 10 images. A background image was recorded to remove background noise. The camera was setup at a 90° angle to the CW laser beam path and to the laser beam polarization. A reference LRS signal was recorded in a dry air flow.

The Rayleigh cross section (when viewed at 90° angle to the laser polarization) is defined as $\sigma_{R,i} = 4\pi^2 (n_i\text{-}1)^2 / N_0^2 \lambda^4$ [5], where n_i is the refractive index for molecule i, N_0 is the number density and λ is the wavelength of the laser radiation. For a completely accurate calculation of the cross sections, the depolarization ratio should also be considered; however, due to the difficulty in finding reliable values for the depolarization ratio at 457 nm, the effect of this was assumed to be negligible in our measurements. This is usually a reasonable assumption for visible laser wavelengths [23,24]. An uncertainty of 2.5% in the Rayleigh cross sections was assumed in order to account for this and other uncertainties in the gas composition in the flames.

The Rayleigh cross section for a mixture becomes a weighted sum of the cross section of each molecule. The temperature was calculated from the LRS scattering intensity I_a and I_f in the air and flame, respectively, as $T_f = T_a \cdot I_a / I_f \cdot \sigma_f / \sigma_a$. Table 3 shows the refractive index for the major species present in the flame, together with the calculated Rayleigh cross sections at 457 nm.

3. Results and discussion

Given the gas composition and relevant gas constants, the gas temperature T in the LITGS crossing point can be calculated from the oscillation frequency f_{osc} and speed of sound $c_s = (\gamma T R_u / M_{gas})^{1/2}$ as

$$T = \frac{f_{osc}^2 \Lambda^2}{R_u (\gamma / M_{gas})} \quad (1)$$

where Λ is the grating spacing, R_u is the universal gas constant, γ is the specific heat ratio and M_{gas} is the molecular weight of the gas.

Figure 2 shows the IR-LITGS signals recorded in Flames 2 and 7, respectively. The measurements are a time-average of 200 IR-LITGS signals recorded at 3231 cm^{-1}, which corresponds to the peaks of 'line 2′ marked in Fig. 3. The inset shows the fast Fourier transform (FFT) of the LITGS signals, revealing the oscillation frequency which is used for temperature measurements. The vertical lines indicate the integration area used for recording the IR-LITGS excitation scan in Fig. 3.

3.1. IR-LITGS excitation scan in a CH_4/H_2/air flame

Figure 3 shows the IR-LITGS excitation scan recorded in Flame 7 at 8 mm HAB. Each point represents the IR-LITGS signal intensity at that wavenumber integrated over the time window as shown in Fig. 2. The lower curve shows the absorption coefficient (σ) at 1800 K simulated using the HITEMP 2010 database [29]. The intensity of the simulated absorption was adjusted to match the overall intensity of the IR-LITGS spectrum and is used for a qualitative identification of the absorption lines.

Comparing the IR-LITGS and absorption spectra, there are many strong absorption lines that are missing in the IR-LITGS spectrum, while other lines in the IR-LITGS scan have much higher intensity than expected from the absorption. These missing lines are present in an IR-DFWM spectrum as previously measured by our group [3], indicating the simulation is correct. The insets in Fig. 3 show a zoom of selected H_2O absorption lines in the spectrum, numbered 1–6. Line 1 contains six separate transitions, and the simulation shows three distinct closely spaced peaks. The first two peaks show a strong IR-LITGS signal, while the third peak is absent in the IR-LITGS scan. Lines 1, 2 and 5 show a strong LITGS signal, while lines 3, 4 and 6 are missing.

It is clear that the absorption coefficient is not the only factor affecting the IR-LITGS signal intensity. Hemmerling et al. [15] investigated how the collisional relaxation and energy transfer processes of O_2 influence the LITGS signal. They showed that the initial part of the O_2-LITGS signal is mostly affected by the rotational energy transfer (RET), which redistributes the rotational population in the excited state to thermal equilibrium. The rotation-resolved LITGS signal was found to be strongly dependent on the type of rotational transition being studied.

Table 4 shows the HITEMP data for lines 1–6. The discrete transitions within a line are labeled a, b, c, etc. The table gives values for the transition wavenumber (v), line intensity (S) at 1500 K, Einstein A coefficient, lower state energy (E) and the

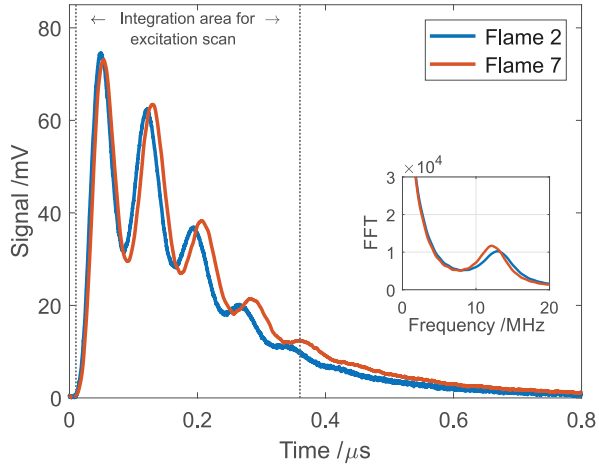

Fig. 2. IR-LITGS signals of the hot water line group (‘line 2′ in Fig. 3) at 3231 cm^{-1} in Flames 2 and 7, respectively. The inset shows the FFT of the signal. The vertical lines indicate the integration area used for the excitation scan.

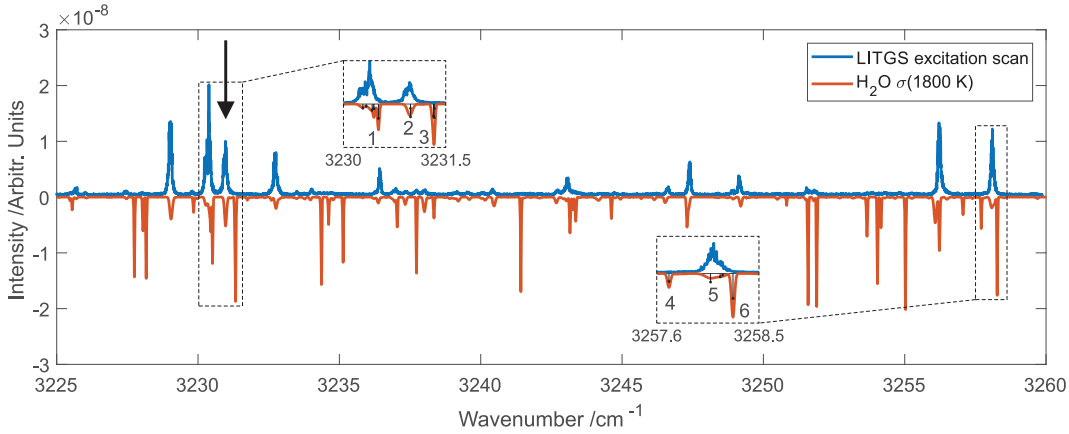

Fig. 3. The upper curve shows the IR-LITGS excitation scan recorded in Flame 7. The arrow indicates ‘line 2′ where the IR-LITGS signals in Fig. 3 were recorded. The lower curve shows the simulated absorption coefficient σ at 1800 K. The intensity of the simulation has been adjusted to match the IR-LITGS intensity. The insets show a zoom of the selected water lines 1–6 in Table 4.

upper and lower vibration and rotation energy levels. The rotational energy levels of H_2O are characterized by three quantum numbers *J*, K_a and K_c, where J represents the total angular momentum and K_a and K_c are projections of J on the axes of inertia [29].

Comparing the rotational quantum numbers *J*, K_a and K_c in the upper and lower state, all transitions have $\Delta J=-1$ and $\Delta K_c=\pm 1$. However, lines 1e-f, 3, 4, and 6 (marked with * in Table 4) have $\Delta K_a=0$. These are also the same lines that are missing in the IR-LITGS excitation scan (or are too weak to be measured with this setup). The transitions 1a-d and lines 2 and 5 have $\Delta K_a=-1$ (transition 1c has $\Delta K_a=-2$) and these lines all show a strong IR-LITGS signal. Analyzing the HITEMP data for the whole spectral range in Fig. 3, it appears that lines with $\Delta K_a\neq 0$ give rise to strong IR-LITGS signals, while transitions with $\Delta K_a=0$ do not show an IR-LITGS signal.

It seems that the main contribution to the IR-LITGS signal arises from RET. The most efficient RET occurs when the quantum number K_a changes during the transition. The energy structure of an asymmetric top molecule like water is complicated. An in-depth analysis of the energy transfer processes in water is outside the scope of this paper. However, it is clear that for IR-LITGS thermometry using water absorption, proper H_2O lines (with $\Delta K_a\neq 0$) must be selected to generate a strong IR-LITGS signal.

Table 4
Spectral data from HITEMP [29] for the H_2O transitions for lines 1–6 in Fig. 3. The columns show the values for transition wavenumber (v), line intensity (S), Einstein A-coefficient, lower state energy (E), and the vibrational and rotational quantum numbers for the upper (') and lower (") energy levels, respectively. Separate transitions within a line are labeled a, b, c, etc. The transitions marked * have $\Delta K_a = 0$, and these lines are not visible in the IR-LITGS excitation scan.

Line	v [cm^{-1}]	S (1500 K)[cm/molecule]	A [s^{-1}]	E [cm^{-1}]	v'	v"	J' K_a' K_c'	$J"$ $K_a"$ $K_c"$
1a	3230.284	$7.67\cdot10^{-22}$	1.585	1718.719	0 0 1	0 0 0	9 3 7	10 5 6
b	3230.333	$2.97\cdot10^{-22}$	3.023	3383.265	1 1 0	0 1 0	9 4 5	10 5 6
c	3230.42	$1.16\cdot10^{-21}$	2.46	1631.383	0 0 1	0 0 0	8 4 4	9 6 3
d	3230.437	$6.62\cdot10^{-22}$	3.044	2918.245	1 0 0	0 0 0	13 4 9	14 5 10
e*	3230.449	$4.77\cdot10^{-22}$	50.02	5471.966	0 0 1	0 0 0	20 4 17	21 4 18
f*	3230.513	$1.43\cdot10^{-21}$	50.11	5471.865	0 0 1	0 0 0	20 3 17	21 3 18
2a	3230.983	$7.74\cdot10^{-22}$	6.511	1789.043	1 0 0	0 0 0	7 7 1	8 8 0
b	3230.983	$2.30\cdot10^{-21}$	6.453	1789.043	1 0 0	0 0 0	7 7 0	8 8 1
3a*	3231.321	$1.29\cdot10^{-21}$	34.75	5035.127	0 0 1	0 0 0	17 8 10	18 8 11
b*	3231.332	$4.33\cdot10^{-22}$	49.89	5713.250	0 0 1	0 0 0	23 0 23	24 0 24
c*	3231.332	$1.30\cdot10^{-21}$	49.96	5713.250	0 0 1	0 0 0	23 1 23	24 1 24
4*	3257.708	$7.62\cdot10^{-22}$	49.76	4855.152	0 0 1	0 0 0	18 5 14	19 5 15
5a	3258.074	$1.38\cdot10^{-21}$	2.974	1631.383	1 0 0	0 0 0	8 5 4	9 6 3
b	3258.159	$5.39\cdot10^{-22}$	3.489	1631.246	1 0 0	0 0 0	8 5 3	9 6 4
c	3258.18	$1.38\cdot10^{-22}$	6.767	4756.394	2 0 0	1 0 0	7 3 4	8 4 5
6*	3258.271	$2.40\cdot10^{-21}$	52.08	4851.821	0 0 1	0 0 0	18 4 14	19 4 15

3.2. Temperature measurement using IR-LITGS

The IR-LITGS temperature measurement depends on the determination of the oscillation frequency of the IR-LITGS signals. A theoretical LITGS signal, based on the model from [30], was fitted to the recorded single-shot IR-LITGS signals in order to retrieve the oscillation frequency in the signals. Figure 4a and b shows single-shot IR-LITGS signals recorded in Flames 2 and 7, respectively, together with a fitted simulated LITGS signal. The insets show the oscillation frequency of the single-shot signal. The single-shot IR-LITGS signal-to-noise ratio was observed to be 800:1 for the weakest recorded signals and better than 5000:1 for the strongest signals, which required the use of ND-filters to avoid saturating the PMT.

The oscillation frequency for the measurement in Flame 7 is lower compared to the measurement in Flame 2, due to the lower flame temperature. 100 single-shot IR-LITGS signals were recorded in each flame, and the flame temperature was calculated from the fitted oscillation frequency according to Eq. (1). The normal distribution of the calculated temperatures for Flame 2 and 7 are shown in Fig. 4c. The measured flame temperatures were 1783 ± 15 K for Flame 2 and 1565 ± 7 K for Flame 7. The precision is computed from the standard deviation of the normal distribution from simulation fits to 100 single-shot LITGS signals recorded in each flame.

The gas composition in Table 2, simulated using the program CEA [22], was used to determine the average molar mass of the molecules in the product zone of the flames, which is necessary for calculating the flame temperature from the IR-LITGS signals using Eq. (1). The heat capacity ratio (γ) in the flames was calculated in the program REFPROP [31], also using the gas composition in Table 2, and γ was evaluated to be 1.257 and 1.276 for Flames 2 and 7, respectively. The temperature uncertainty given in Fig. 4c reflects the single-shot precision of the measurement, which is better than 1% of the calculated flame temperature.

3.3. Product zone temperature

Figure 5 shows temperatures measured both from IR-LITGS and LRS for flames 1–8. The IR-LITGS temperature in each flame is an average of the temperature derived from 100 single-shot IR-LITGS signals. The calculated temperatures are lower compared to the adiabatic flame temperatures for these flames, which is probably due to heat losses to the burner and the bluff-body stabilizer. The measurements were performed in the product zone of the flame and at 8 mm HAB, and the LRS measurements also showed that the temperature between 7 and 9 mm HAB decreased with approximately 300 K/mm, which could be due to radiative heat losses or other heat losses to the surroundings. As can be seen in Fig. 5, there is a good agreement in the temperature measurements between the two techniques. Because of the temperature gradient in the measurement point, there could be up to ± 75 K difference in the flame temperature measured by LRS and IR-LITGS due to the approximately ± 0.25 mm uncertainty in the exact HAB in the IR-LITGS measurement. A small error in the precise value of the gas constants γ/M_{gas} used in the IR-LITGS temperature measurement could also be a factor.

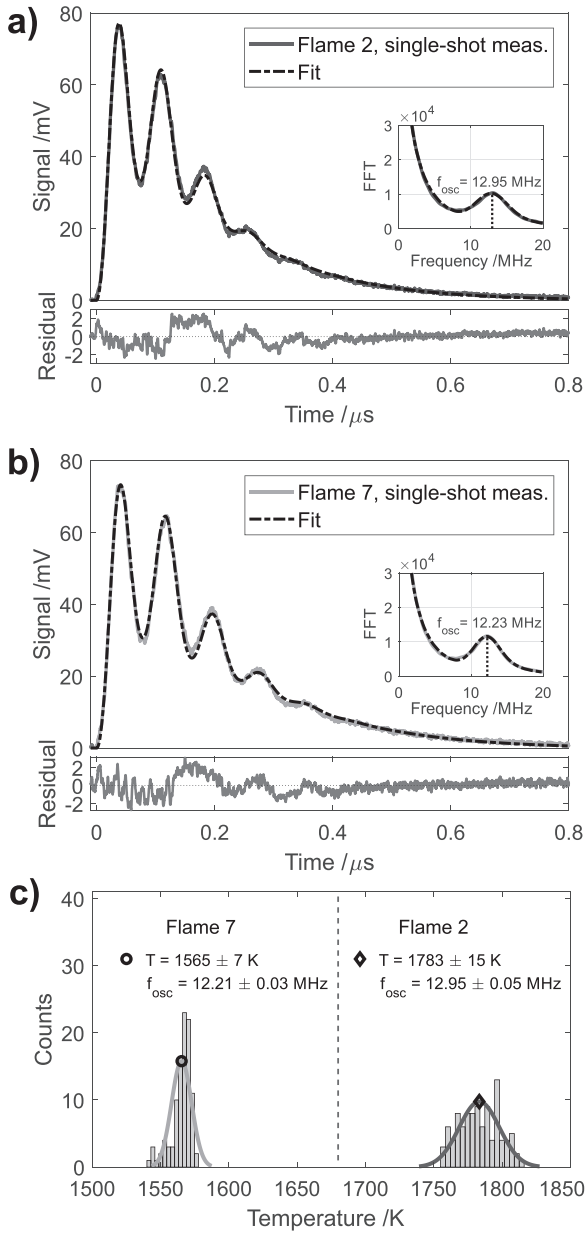

Fig. 4. Single-shot IR-LITGS signals of line 2 recorded at 3231 cm^{-1} in a) Flame 2 and b) Flame 7. From the simulation fit the precise oscillation frequency can be obtained (inset in a) and b)) for temperature calculation. The normal distribution of 100 single-shot measurements of the IR-LITGS temperature for the two flames is shown in c). A single-shot precision better than 1% is obtained for the flame temperature measurement.

Both IR-LITGS and LRS require an initial calibration at a known temperature. For LRS, the calibration was performed in a room-temperature dry air flow, and the calibration was used to convert the LRS measurement in the flame into a quantitative temperature measurement. For IR-LITGS, a calibration measurement was performed in a room-temperature gas flow of N_2 containing trace concentrations of C_2H_2, to determine the precise grating spacing in this setup. IR-LITGS gives a direct measurement of the speed of sound in the flame, which can be used to calculate the flame temperature provided the gas constants in the flame are known. For LRS, the gas composition is needed to calculate the Rayleigh cross section (σ). The gas composition presented in Table 2 of the four

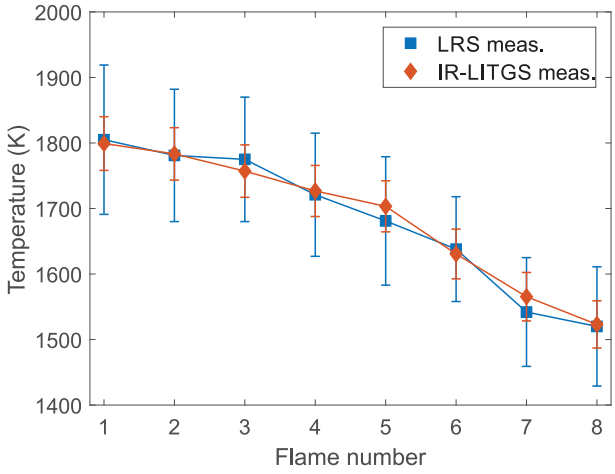

Fig. 5. Flame temperatures at 8 mm above the burner in flames 1–8, measured with LRS and IR-LITGS.

major product species, N_2, O_2, H_2O and CO_2 were used in the temperature calculation for both techniques. Additional minor molecular species had no significant impact on the temperature calculations. This indicates that for flames 1–8, which have $0.6 \leq \Phi \leq 1.05$, the bulk gas thermophysical properties are correlated with these four major species. However, as shown in [19], at fuel-rich flame conditions, the accurate mole fraction of hydrogen needs to be included in the gas composition for accurate IR-LITGS temperature measurements.

The error bars in the IR-LITGS temperature in Fig. 5 are affected by the uncertainty in the gas constants γ/M_{gas} (estimated to be $\pm$ 2%), and the uncertainty in determining the grating spacing Λ, (around $\pm$ 1 μm). This results in an overall accuracy of 2.5% in the IR-LITGS temperature measurement. The error bars of the LRS measurement take into consideration the intensity fluctuation in the LRS signal intensity, as well as the uncertainty in the gas composition and the calculated Rayleigh scattering cross sections. This results in a total uncertainty of around 7% of the calculated product zone flame temperature. There are many LRS measurements with better precision than this simple measurement (see, e.g. [6,32,33]) but the main target of this article is the IR-LITGS measurements.

4. Conclusions

In this work, we investigated the feasibility of IR-LITGS in atmospheric flat CH_4/H_2/air flames by probing hot water absorption lines around 3.1 μm. The measurements were performed in the product zone where the main combustion product water is present. Measurements can also be performed in the reaction zone as long as water is present in sufficient concentrations, although quantitative measurements are limited by the spatial resolution and complicated by the uncertainty in the gas composition. The excellent signal-to-noise ratio enables temperature measurements with high precision and accuracy in single-shot approach. By using a mid-infrared pump laser, it was possible to achieve an IR-LITGS setup with the large grating spacing of 63.5 μm, leading to relatively long signal durations of the transient IR-LITGS signals even in the atmospheric pressure flames. A repetitive single-shot temperature precision of better than 1% was achieved in the laminar flames, and the accuracy of the temperature measurement was estimated to be 2.5%. This is comparable to typical CARS experiments that have demonstrated ~1–1.5% single-shot precision for flame thermometry (see e.g. [34–36]) and 3–5% accuracy for fs/ps rotational CARS [34] or 3.3% accuracy for fs/ps vibrational CARS [35]. While CARS is still more applicable in environments where the gas composition cannot be accurately estimated, LITGs is less sensitive to quenching and line-broadening. The reliability of the IR-LITGS measurements were further confirmed by the good agreement with LRS measurements, where both techniques provide absolute temperature measurements. An IR-LITGS excitation scan of the hot water lines in the flame revealed that some ro-vibrational transitions of water do not exhibit an IR-LITGS signal, which is likely due to less efficient collisional energy transfer for these absorption lines. This implies that a selection of proper water absorption lines is needed for IR-LITGS measurements.

In conclusion, this paper shows the potential for IR-LITGS technique for precise and accurate flame temperature measurements in atmospheric pressure flames. The IR-LITGS temperature measurement is expected to improve even more for measurements in high pressure environments, such as

gas turbines or reciprocal engines. For turbulent conditions, the applications are currently limited to characteristic length and time scales larger than the spatial resolution $16 \times 0.5 \times 0.5\,mm^3$ and the $0.5\,\mu s$ LITGS signal duration. IR-LITGS also has good potential for temperature measurements in sooty or particle-laden combustion environments, since particle scattering has a small effect on mid-IR laser beams.

Declaration of Competing Interest

We declare that we have no competing interests.

Acknowledgment

We thank for the support from the Swedish Energy Agency through the KC-CECOST project, the Knut & Alice Wallenberg foundation, the Swedish Research Council (VR) and the European Research Council (ERC) through the Advanced Grant TU-CLA.

References

[1] J.M. Seitzman, R.K. Hanson, P.A. Debarber, C.F. Hess, *Appl. Opt.* 33 (1994) 4000–4012.
[2] J. Borggren, W. Weng, A. Hosseinnia, P.-.E. Bengtsson, M. Aldén, Z. Li, *Appl. Phys.* B 123 (2017) 278.
[3] Z.W. Sun, Z.S. Li, B. Li, M. Aldén, *J. Raman Spectrosc.* 42 (2011) 1828–1835.
[4] S. Roy, J.R. Gord, A.K. Patnaik, *Prog. Energy Combust. Sci.* 36 (2010) 280–306.
[5] F.-.Q. Zhao, H. Hiroyasu, *Prog. Energy Combust. Sci.* 19 (1993) 447–485.
[6] J. Zetterberg, Z. Li, M. Afzelius, M. Aldén, *Appl. Spectrosc.* 62 (2008) 778–783.
[7] J. Kiefer, P. Ewart, *Prog. Energy Combust. Sci.* 37 (2011) 525–564.
[8] E.B. Cummings, M.S. Brown, P.A. DeBarber, H.G. Hornung, *Opt. Lett.* 20 (1995) 1577–1579.
[9] A. Stampanoni-Panariello, B. Hemmerling, W. Hubschmid, *Appl. Phys. B: Lasers Opt.* 67 (1998) 125–130.
[10] A. Luers, A.-.L. Sahlberg, S. Hochgreb, P. Ewart, *Appl. Phys. B: Lasers Opt.* 124 (2018) 43.
[11] H. Latzel, A. Dreizler, T. Dreier, et al., *Appl. Phys. B: Lasers Opt.* 67 (1998) 667–673.
[12] F. Förster, C. Crua, M. Davy, P. Ewart, *Combust. Flame* 199 (2019) 249–257.
[13] B. Williams, M. Edwards, R. Stone, J. Williams, P. Ewart, *Combust. Flame* 161 (2014) 270–279.
[14] F.J. Förster, S. Baab, G. Lamanna, B. Weigand, *Appl. Phys. B: Lasers Opt.* 121 (2015) 235–248.
[15] B. Hemmerling, D.N. Kozlov, *Chem. Phys.* 291 (2003) 213–242.
[16] A. Hayakawa, T. Yamagami, K. Takeuchi, et al., *Proc. Combust. Inst.* 37 (2019) 1427–1434.
[17] F. De Domenico, T.F. Guiberti, S. Hochgreb, W.L. Roberts, G. Magnotti, *Combust. Flame* 205 (2019) 336–344.
[18] A.L. Sahlberg, J. Kiefer, Z.S. Li, M. Aldén, *Appl. Spectrosc.* 70 (2016) 1034–1043.
[19] A.-.L. Sahlberg, D. Hot, J. Kiefer, M. Aldén, Z. Li, *Proc. Combust. Inst.* 36 (2017) 4515–4523.
[20] Z.S. Li, C.H. Hu, J. Zetterberg, M. Linvin, M. Aldén, *J. Chem. Phys.* 127 (2007) 084310 084310-.
[21] Z.S. Li, M. Rupinski, J. Zetterberg, Z.T. Alwahabi, M. Aldén, *Chem. Phys. Lett.* 407 (2005) 243–248.
[22] S. Gordon, B.J. McBride, *NASA Reference Publication 1311: Computer Program for Calculation of Complex Chemical Equilibrium Compositions and Applications*, National Aeronautics and Space Administration, 1996.
[23] J.A. Sutton, J.F. Driscoll, *Opt. Lett.* 29 (2004) 2620–2622.
[24] J. Fielding, J.H. Frank, S.A. Kaiser, M.D. Smooke, M.B. Long, *Proc. Combust. Inst.* 29 (2002) 2703–2709.
[25] E.R. Peck, B.N. Khanna, *J. Opt. Soc. Am.* 56 (1966) 1059–1063.
[26] W.C. Gardiner, Y. Hidaka, T. Tanzawa, *Combust. Flame* 40 (1981) 213–219.
[27] J. Zhang, Z.H. Lu, L.J. Wang, *Appl. Opt.* 47 (2008) 3143–3151.
[28] J.G. Old, K.L. Gentili, E.R. Peck, *J. Opt. Soc. Am.* 61 (1971) 89–90.
[29] L.S. Rothman, I.E. Gordon, R.J. Barber, et al., *J. Quant. Spectrosc. Radiat. Transf.* 111 (2010) 2139–2150.
[30] D.N. Kozlov, J. Kiefer, T. Seeger, A.P. Fröba, A. Leipertz, *J. Phys. Chem. B* 118 (2014) 14493–14501.
[31] E.W. Lemmon, I.H. Bell, M.L. Huber, M.O. McLinden, *NIST Standard Reference Database 23: Reference Fluid Thermodynamic and Transport Properties-REFPROP* (2013) Standard Reference Data Program.
[32] N.J. Kempema, M.B. Long, *Appl. Opt.* 53 (2014) 6688–6697.
[33] E. Kristensson, A. Ehn, J. Bood, M. Aldén, *Proc. Combust. Inst.* 35 (2015) 3689–3696.
[34] S.P. Kearney, *Combust. Flame* 162 (2015) 1748–1758.
[35] J.D. Miller, M.N. Slipchenko, T.R. Meyer, H.U. Stauffer, J.R. Gord, *Opt. Lett.* 35 (2010) 2430–2432.
[36] D.R. Richardson, R.P. Lucht, W.D. Kulatilaka, S. Roy, J.R. Gord, *Appl. Phys. B: Lasers Opt* 104 (2011) 699.